Volume 3 | Number 26 | 14 July 2015 | Pages 6575–6934

Journal of Materials Chemistry C

Materials for optical, magnetic and electronic devices

www.rsc.org/MaterialsC

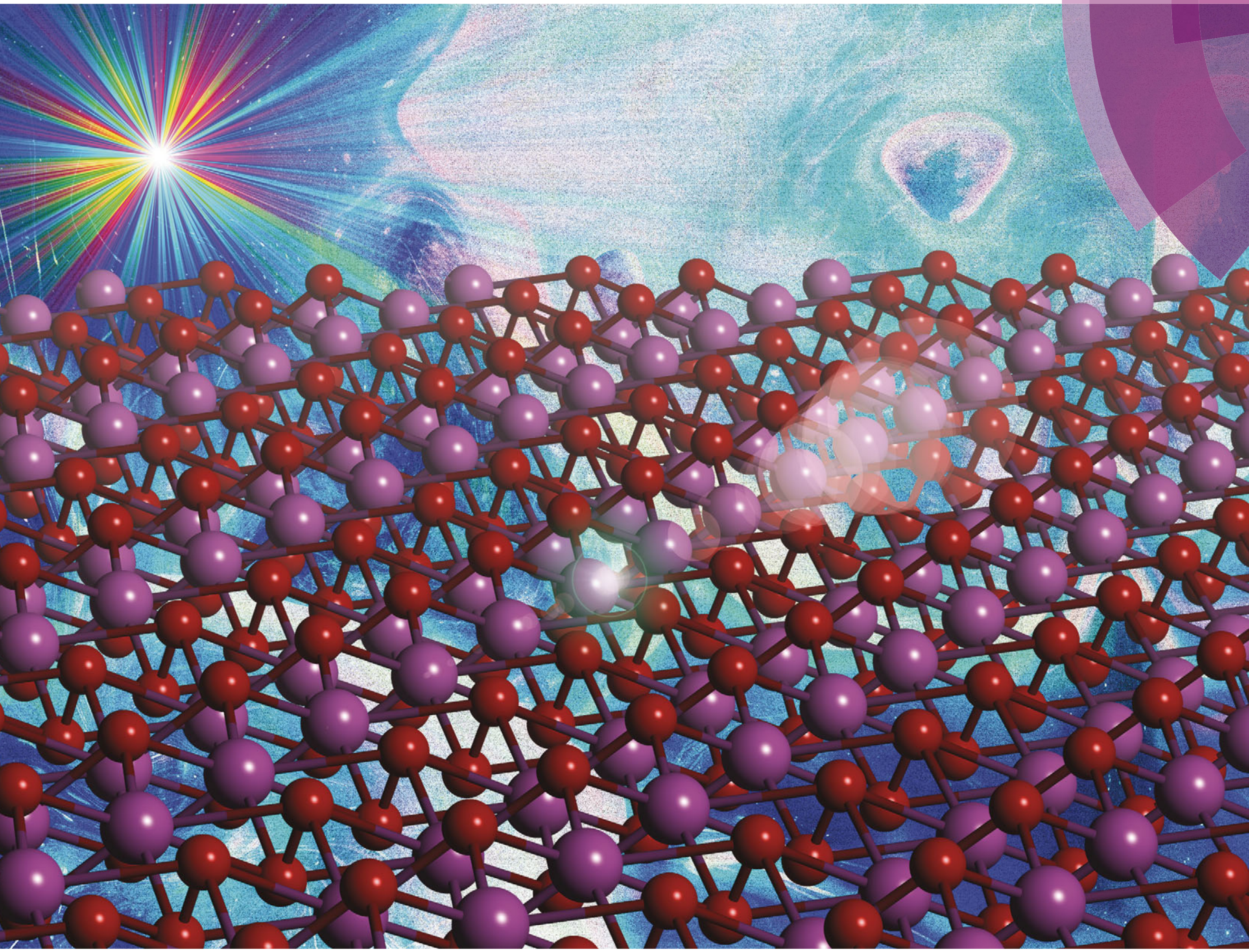

ISSN 2050-7526

ROYAL SOCIETY OF CHEMISTRY

PAPER

G. C. Loh and Ravindra Pandey

Versatile electronic properties of atomically layered ScO_2

Journal of
Materials Chemistry C

PAPER

View Article Online
View Journal | View Issue

Cite this: *J. Mater. Chem. C*, 2015, **3**, 6627

Versatile electronic properties of atomically layered ScO_2†

G. C. Loh*[a][b] and Ravindra Pandey*[a]

In recent years, graphene and transition metal dichalcogenides (TMDs) have been at the forefront of candidate materials for next-generation electronic devices. In this study, we will consider transition metal oxides (TMOs), which are a class of materials that can exist in two-dimensional geometries, but exhibit unique properties due to the strong correlation between electrons. Density functional theory calculations under the generalized-gradient approximation with on-site Coulomb interactions (GGA + *U*) are performed to investigate the (a) geometry, (b) energetics, (c) electronic properties, (d) magnetic properties, and (e) chemical bonding of a layered TMO–scandium dioxide (ScO_2) in its octahedral (T) and hexagonal (H) phases. The T-phase is a non-magnetic wide-band gap semiconductor with a band gap of 3.75 and 3.73 eV for the monolayer and bilayer, respectively. The H-phase monolayer is an anti-ferromagnetic (AFM) metal while the bilayer is metallic and has a ferromagnetic (FM) and an AFM configuration, which degenerate in energy. The metallicity and magnetic coupling between atoms in the H-phase are predominantly governed by the O-p_z states. The analysis of the chemical topology using the quantum theory of atoms in molecules (QTAIM) shows that the Sc–O bonds are highly ionic in character. Born effective charge (Z^*) analysis suggests that the H-phase monolayer has more uniform chemical bonding. Furthermore, T- and H-phase bilayers respond differently to strain applied normal to the material surface; for the former, the band gap increases and then decreases with the increase of tensile strain, whereas the latter shows a metal → semiconductor → metal transition as a larger tensile strain is applied. The mechanisms for such responses are inherently different in the two phases: in the T-phase, it is due to the shift of the lowest unfilled O-p_z band, and in the H-phase, it is attributed to the transformation in shape of the bands close to the Fermi level. The versatility of the electronic properties of ScO_2 in its different phases and forms (monolayer and bilayer) can thus be exploited in devices at the nanoscale.

Received 18th April 2015,
Accepted 27th May 2015

DOI: 10.1039/c5tc01096a

www.rsc.org/MaterialsC

1. Introduction

Since the realization of graphene as a free-standing and stable two-dimensional (2D) material,[1] its plenitude of unique and intriguing properties[2–6] has captivated the interest of the scientific community in the past decade. However, although it has been widely-publicized as the next-generation electronic material[7] that will replace silicon, it lacks a gap in its electronic band structure, *i.e.* it is a semi-metal. A band gap has to be induced by either doping,[8] applying an external electric field,[9] or cutting it into nanoribbons[10] to render graphene suitable as a semiconducting material in transistors or other electronic devices. It has nonetheless shown glimpses of potential due to its extremely high carrier mobility[7] and in other fields such as biological engineering,[11] and energy storage.[12] Despite its Achilles' heel, with recent leaps and bounds in progress in its synthesis[13–16] it is not surprising that the scope of attention has been widened in the search for alternative 2D materials, which can rival or even surpass the performance of graphene while behaving as a semiconductor for electronic applications. One such class of materials is the transition metal dichalcogenides (TMDs). In fact, some of these materials are not novel as their bulk forms have been investigated many decades ago; for instance, molybdenum disulphide (MoS_2) has been used as an excellent lubricant due to the van der Waals (vdW) interaction between its layers.[17] However, the 2D forms of the TMDs, which have only been carefully examined after the emergence of graphene, have indeed shown promising traits. An outstanding example is monolayers of MoS_2, which have a large carrier mobility[18] and high current-carrying capacity,[19] whereas other intensively-studied TMDs such as the tungsten-based dichalcogenides (WS_2, WSe_2)

---

[a] *Department of Physics, Michigan Technological University, Houghton, Michigan 49931, USA. E-mail: jgloh@mtu.edu, pandey@mtu.edu*

[b] *Institute of High Performance Computing, 1 Fusionopolis Way, #16-16 Connexis, Singapore 138632*

† Electronic supplementary information (ESI) available. See DOI: 10.1039/c5tc01096a

have exhibited similar superior electrical performance.[20] However, not all 2D TMDs are semiconducting; some have been found to be electrically insulative[21,22] or metallic.[23,24] The diversity of their electrical characteristics expands the range of applications that they can be employed in.

Transition metal oxides (TMOs) are compounds that consist of transition metal and oxygen atoms in variable proportions and arrangements. In the MX_2 manifold (M: transition metal; X: chalcogen, for *e.g.* S, Se, O) they are also called transition metal dioxides, and closely resemble TMDs in geometry with the atoms bonded together in a X–M–X sandwich-like arrangement (hereafter named as MX_2-TMDs and MX_2-TMOs). The sub-layers of atoms are subsequently stacked to form graphite-like multilayers or the bulk structure. The M atoms are positively charged, *i.e.* cations, and the X atoms are negatively charged, *i.e.* anions. Monolayer MX_2-TMDs/MX_2-TMOs are typically in either a honeycomb hexagonal (H) structure with D_{3h} point group symmetry or a centered honeycomb octahedral (T) structure with C_{3v} symmetry. Some of them can exist in either form, while others are not stable as a freestanding structure.[25] In the H-phase, the two X sub-layers are aligned with each other in the direction normal to the surface, while in the T-phase the M atoms are trigonal and prismatic with respect to the X atoms. The intralayer M–X bonds are highly covalent in character.

Despite the similarities between the geometries of MX_2-TMDs and MX_2-TMOs, electrons in the two types of material behave very differently. TMOs, in general, are a unique material class aptly named as strongly correlated materials in which Coulomb interactions between certain electrons are considerably stronger than those in conventional materials. Other types of such systems include cuprate superconductors[26] and heavy-electron compounds.[27] Due to the strong correlation effects, the electronic band structure differs from that predicted by the usual band theory. In particular, in all forms of TMO, the 2p orbitals of the oxygen anion overlap and form multiple bands in the valence band near the Fermi level, while the sparsely populated conduction band is predominantly made up of d-orbitals on the transition metal cation.[28] As the d-orbitals are small,[29] the interaction effects between these orbitals and others are enhanced and their overlap with other orbitals is decreased, which then reduces the kinetic energy of the electrons. If the correlation effects are sufficiently strong, the mobility of the conduction electrons is curtailed to the extent of the formation of a band gap.

Essentially, the emergence of strong correlation effects poses a challenge to our understanding of solids as many novel and unusual properties are observed in these electron systems, including half-metallicity,[30] metal–insulator transition,[31] colossal magnetoresistance (CMR),[31] high-temperature superconductivity,[32] and multiferroicity.[33] These phenomena indeed reveal a new ‘world’ of solid state physics, but at the same time, the intricacy of electron interactions in these systems inevitably brings about a severe technical problem in the calculations of their electronic structure. Typically, the theoretical tool for solving the quantum many-body problem is density functional theory (DFT) in the local density approximation (LDA) in which the many-body system is mapped into a non-interacting one with a one-electron exchange correlation potential, thereby mimicking a homogeneous electron gas.[34] However, in strongly correlated systems such as TMOs which contain localized d/f electrons on the transition metal cations and a distinct band gap, LDA predicts a partially d/f band with metallic character and itinerant electrons. Therefore, LDA fails to accurately describe the electronic structure of these systems.

How do we then represent the electron interaction more correctly in these unique materials? Many approaches have been subsequently developed to rectify the shortcomings of LDA, including the Hartree–Fock (HF) method,[35] the GW approximation,[36,37] the self-interaction correction (SIC) method,[38] and the LDA + U method.[39] Despite improvements on LDA, some of these methods are still imprecise in one way or another. For instance, although the exchange potential in the HF formulation contains a term that cancels out the unphysical self-interaction between electrons, the Coulomb interaction is unscreened and therefore considerably stronger than in realistic scenarios. Hence, predicted band gaps are typically a few times larger than experimental values. On the other hand, the LDA + U method ameliorates the problem; in addition to including the screening effect, it couples the calculations with an additional orbital-dependent Hubbard repulsion term to correct for the unphysical self-interaction between electrons in exchange and correlation functionals that have not been treated exactly. Due to its reasonable accuracy and ease of use in many computational packages, the LDA + U method has become one of the more popular approaches for describing strong correlation effects.

The structural stability of some MX_2-TMOs such as vanadium dioxide (VO_2)[40] and chromium dioxide (CrO_2)[41–44] has recently been affirmed experimentally. The stability of VO_2 allotropes has been found to be temperature-dependent, and a metal-to-insulator transition is observed in the allotropes with a change in temperature.[40] CrO_2 is half-metallic in character and has been investigated mainly for spintronic applications.[41–44] Among the transition metals, scandium (Sc) is the lightest. Due to its rare availability and the difficulties in its preparation after extraction, relatively little is known about the compounds it can form or the properties of these compounds. In fact, the only familiar one to us is bulk scandium(III) oxide (Sc_2O_3), which is the primary form of Sc produced by the mining process that is mainly used as a strengthening material in alloys.[45]

Is this the only existing form of Sc oxide? Perhaps more important is the question: are there other useful Sc oxides? Moreover, can Sc and O atoms form a stable MX_2 monolayer or bilayer? Some of these questions have been addressed by Ataca and coworkers;[25] using DFT calculations in the LDA approximation, they have suggested that ScO_2, together with 7 other MX_2-TMOs out of the 11 they investigated, are stable and freestanding in the single-layer 2D form. These other MX_2-TMOs include VO_2, CrO_2, manganese dioxide (MnO_2), iron dioxide (FeO_2), nickel dioxide (NiO_2), molybdenum dioxide (MoO_2), and tungsten dioxide (WO_2). Some of them are predicted to be stable as a monolayer in either the T-(NiO_2) or H-phase (VO_2, CrO_2, FeO_2, MoO_2, and WO_2), or even both phases (ScO_2 and MnO_2). To make a coherent comparison between the properties of different MX_2-TMO/TMD monolayers in their T- and H-phases, strong correlation effects in the MX_2-TMOs are not accounted for in most of their calculations. A separate study was then done to take correlation effects into consideration to explore how the strength of correlation affects the band gap of a few layered TMOs.[25] It is predicted that the T-phase monolayer undergoes a transformation from a half-metal into a semiconductor when the correlation effects are adequately strong.

What remains unanswered mainly concerns the ScO_2 bilayer – is it stable as a freestanding structure? If so, does the presence of the additional layer modulate the geometry within each layer? Furthermore, are the electronic properties predicted in ref. 25 unique to ScO_2 in the monolayer form? How does H-ScO_2 behave electronically with the inclusion of strong correlation effects? In this work, we address the aforementioned questions in detail by first-principles calculations using the generalized-gradient approximation with on-site Coulomb interaction (GGA + U). The geometry of ScO_2 and its electronic and magnetic behaviour are compared with those under the LDA and LDA + U schemes in ref. 25. Only the most common phases of octahedral (T) and hexagonal (H) are studied. It is to be noted that the on-site interaction in ScO_2 has not been quantified by experimental measurements and therefore parameters have not been established. In this regard, only a qualitative comparison of the findings is possible. In addition, the chemical bonding of the different configurations of ScO_2 is analyzed using the quantum theory of atoms in molecules (QTAIM) and the Born effective charge tensor Z^*. Thereafter, we probe the interaction strength between layers in the bilayers indirectly by applying strain in the direction normal to the material surface, and then examine the response of the electronic properties to the applied strain. The mechanism that results in such a response is then delineated.

2. Computational model

The ScO_2 monolayer is simulated by a (4×4) supercell containing 4 Sc and 8 O atoms. In both T- and H-phases, a Sc sub-layer is sandwiched between two O sub-layers. In the former, six O atoms are arranged around each Sc atom in a distorted octahedral manner (Fig. 1(a)) while in the latter, the atoms are bonded together in a buckled honeycomb configuration (Fig. 1(c)). Due to strong correlation effects, the T-phase lattice is distorted and the Sc atoms form zigzag rows, which are reminiscent of the dimerized Re chains in rhenium disulphide (ReS_2).[46,47] Note that this distortion has not been reported in ref. 25. These Sc atoms within the zigzag rows are spaced closer to each other as compared to that with Sc atoms in a neighboring row. In this study, we shall investigate whether these Sc atoms are bonded together in chains in the same way as Re atoms in ReS_2. The calculated bond length in the T-phase ranges from 2.05 to 3.10 Å, while that in the H-phase is approximately 2.19 Å. In the T-phase, the separation between Sc zigzag rows is about 3.10 Å, whereas the separation between sub-layers in the T-phase (H-phase) is approximately 0.74 (1.11) Å. The structural stability of the monolayer is expressed by the formation energy, which is defined as the difference between the total energy of the system and the sum of the energy of its constituents,

$$E_{\mathrm{f}} = E_{\mathrm{ScO_2}} - \sum_{\alpha=\mathrm{Sc,O}} n_\alpha E_\alpha \tag{1}$$

where $E_{\mathrm{ScO_2}}$ is the total energy of the monolayer, n_α is the number of atoms of a particular element α and E_α is the energy of a single atom of that element α. The formation energy of the monolayer is calculated to be −2.24 eV per atom, relative to −1.84 eV per atom for H-phase monolayer, *i.e.* T-ScO_2 monolayer is more stable. As a comparison, ref. 25, which uses a different formalism, reports values of −2.67 and −2.61 eV per atom for the T- and H-phase, respectively. Nonetheless, both studies find the T-phase of ScO_2 monolayer to be more stable.

The ScO_2 bilayer is formed by stacking one O–Sc–O monolayer on top of another (Fig. 1(b) and (d)). The interlayer separation is approximately 1.77 Å in the T-phase. In the H-phase, the honeycomb lattice is distorted, with rippling of sub-layers. Due to a difference in the lattice symmetry, the closest neighbour pairs between layers are not the same for both phases. In the T-phase, alternating pairs of Sc–O are neighbours, but in the H-phase, they are O–O atoms. In the latter, at points whereby the sub-layers are at their furthest apart, the separation is about 2.48 Å; it is 1.46 Å at their nearest. The formation energies of the T- and H-ScO_2 bilayer are calculated to be −2.46 and −2.04 eV per atom, respectively. In other words, akin to the case of the monolayers, the T-phase bilayer is more stable than the H-phase bilayer. The bilayers are also more stable than the monolayers. Furthermore, to provide a more comprehensive picture of ScO_2 in its various configurations and to give a prediction of its microscopy images, we have performed multislice simulations[48,49] to calculate HA-ADF (high-angle annular dark-field) and TEM (transmission electron microscopy) images together with its average (Z-number × Debye–Waller factor)^2 plot (Fig. 1).

Calculations based on density functional theory (DFT) were performed with the VASP (Vienna Ab Initio Simulation Package) program and the implementation of projector augmented-wave (PAW) pseudopotentials[50] (with an energy cutoff of 400 eV). The Perdew–Burke–Ernzerhof (PBE) exchange–correlation functional in the generalized gradient approximation (GGA)[51] was used. Dispersion correction was included in the calculations by the DFT-D2 approach of Grimme.[52] The Brillouin zone was sampled with a $(19 \times 19 \times 1)$ k-point mesh using the Monkhorst–Pack scheme.[53] The structures were optimized until the forces (as calculated by the Hellmann–Feynman formalism[54,55]) were less than 10^{-5} eV Å^{-1}. In the supercell, the structure is separated from its periodic image in the direction perpendicular to the surface by a vacuum region of 12 Å. Dipole corrections were applied in the direction perpendicular to the material surface to avoid interactions between periodically repeated images.

In our calculations, the Hubbard corrections are carried out using the Dudarev scheme,[56] in which the effective difference of the on-site Coulomb repulsion term U and the exchange parameter J is used to correct for the strong correlation effects.

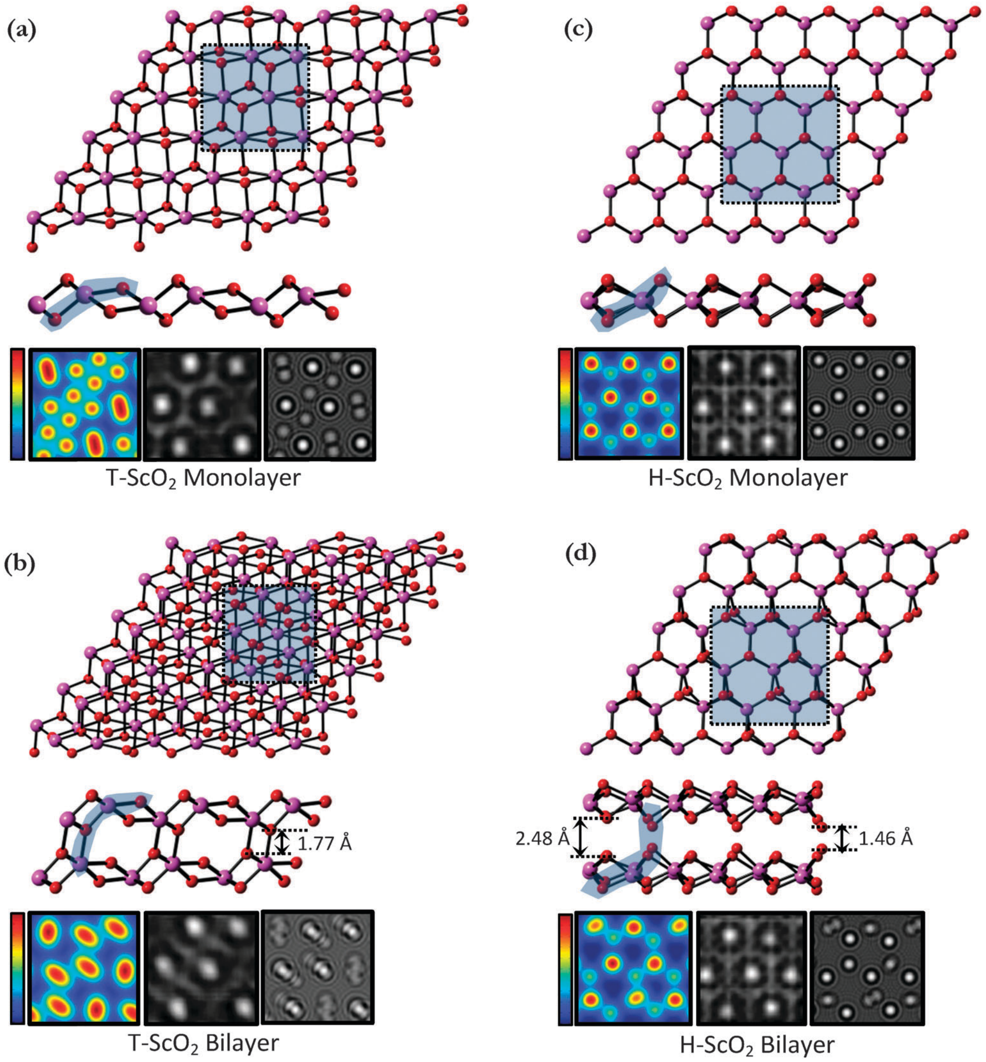

Fig. 1 (a) T-ScO$_2$ monolayer, (b) T-ScO$_2$ bilayer, (c) H-ScO$_2$ monolayer, (d) H-ScO$_2$ bilayer. For each panel, the top view, side view, and multislice simulation images are shown. Top and side views: atoms in purple are Sc, and red are O; the dashed boxes mark the regions in which the multislice simulations are performed; the shaded regions in the side views illustrate the atoms studied in the QTAIM analyses in Section 3.4. Multislice simulations: simulated average (*Z*-number × Debye–Waller factor)^2 plot, with the color bar denoting the magnitude in arbitrary units; simulated HA-ADF image; simulated TEM image.

In this scheme, double-counting is accounted for by the fully localized limit (FLL) approximation[57–59] such that the orbital occupation numbers $n_{i,m}^{\sigma}$ is 0 or 1 and the double-counting term is

$$E_{d-c}\left(n_{i,l}^{\sigma}\right) = \sum_{i,l}\frac{U_{i,l}}{2}N_{i,l}\left(N_{i,l}-1\right) - \sum_{i,l}\frac{J_{i,l}}{2}N_{i,l}^{\sigma}\left(N_{i,l}^{\sigma}-1\right) \quad (2)$$

where $N_{i,l}^{\sigma} = \sum_{m} n_{i,m}^{\sigma}$ is the number of electrons with the spin σ at orbital l of atom i, and $N_{i,l}$ is the total occupation number. The total energy is

$$E_{\mathrm{GGA}+U} = E_{\mathrm{GGA}} + \sum_{i,l}\frac{U_{i,l}-J_{i,l}}{2}\sum_{\sigma}\left[2Tr\left(n_{i,l}^{\sigma}\right) - 2Tr\left(n_{i,l}^{\sigma}n_{i,l}^{\sigma}\right)\right] \quad (3)$$

The values of U and J for both phases have not yet been affirmed in theoretical studies and there are no prior experimental measurements of the band gap of the material. Therefore, we can only approach the problem in a different way – a test is first conducted. ref. 25 has reported the opening of a band gap in the T-phase monolayer above the value $U - J = 4$. To make a direct comparison between the LDA/LDA + U and GGA + U schemes, $U - J$ is varied from 0 to 5 eV (0, 1, 3, 5 eV) to study their effect on the band structure of T- and H-phase monolayers. At $U - J = 0$, the T-phase monolayer is a half-metal (Fig. S1, see ESI†). At $U - J \geq 1$, it becomes a wide-band gap semiconductor. On the other hand, the H-phase monolayer remains metallic from $0 \leq U - J \leq 3$, and transforms to become a half-metal at $U - J = 5$ (Fig. S2, ESI†). Considering that the thrust of this study is to examine the material at reasonable Hubbard parameters and compare its properties under the GGA + U formalism with those under LDA/LDA + U, the value of $U - J$ is chosen to be 5 eV for Sc-d and O-p orbitals.

To partition the continuous charge density among the atoms in the system, Bader's atoms in molecules theory[60–64] is implemented such that the atomic basin is determined at the zero flux surface around the atom. This surface is observed in the two-dimensional sense at which the charge density is at a minimum perpendicular to the system surface. Therefore, the total electronic charge of each atom can be defined. The Born effective charges tensor, Z^*, of each atom is computed by density functional perturbation theory (DFPT) (also known as the linear response method) with an external electric field.[65,66]

3. Results and discussion

3.1 Interlayer bonding: deformation charge density & Bader analysis

Sc has an electron configuration of $[Ar]3d^1 4s^2$ and O has an electron configuration of $1s^2 2s^2 2p^4$; Sc has 1 unpaired 3d electron and O has 2 unpaired 2p electrons. As O is more electronegative than Sc (O: 3.44, S: 1.36 by Pauling[67]), O tends to attract electrons from Sc. Indeed, this is demonstrated by the deformation charge density of ScO_2 in its various forms (monolayer and bilayer) and phases (T and H) (Fig. 2). The contour isovalue is set at 0.02 e Å^{-3}. Interestingly, unlike graphene or 2D TMDs in which layers are coupled by vdW interactions, charges are transferred between different layers in the bilayers (yellow: accumulation; purple: depletion), *i.e.* chemical bonds are formed between layers. In the T-phase bilayer, the interlayer bond has a strong ionic character due to the distinct demarcation of the accumulation and depletion regions, whereas in the H-phase bilayer, the bond is more covalent as the charge transfer regions are generally symmetric between the stacked O atoms.

To quantify and substantiate the abovementioned discussion, Bader's charge analysis[60–64] is carried out. In the T-ScO_2 monolayer, Sc loses 2.17 e per atom and O gains 1.08 e per atom. In the H-phase monolayer, the amount of charges transferred is slightly less (Sc: −2.15; O: +1.07 e per atom). On the other hand, in the T-phase bilayer, the charge transfer is greater (Sc: −2.19; O: +1.09 e per atom) than in the monolayer. This is likely due to additional transfer of charges between layers (Fig. 2). In contrast, depletion of charges between layers in the H-phase bilayer diminishes the exchange of charges between layers, and hence the average charge transfer is less (Sc: −2.13; O: +1.06 e per atom).

3.2 Electronic properties: density of states & band structure

The atom-projected atomic density of states (DOS) is calculated to characterize the nature of the electronic states of ScO_2 in its various configurations (Fig. 3). Both monolayers and bilayers of the T-phase are wide-band gap semiconductors, with band gaps of 3.75 and 3.73 eV, respectively, while the H-phase monolayer and bilayer are metallic. Furthermore, the energy levels of the states in the bilayers deviate only slightly from those in the monolayers. In comparison, ref. 25 reports that the T-phase monolayer is half-metallic under the LDA scheme, but has a small band gap when the Coulomb repulsion term U is greater than approximately 4 eV. In the same study, the H-phase monolayer is a semiconductor with a band gap of 1.05 eV when calculated with the bare LDA approximation. Note that unlike for the T-phase, the calculation for the H-phase is only performed with the bare LDA approximation and strong correlation effects

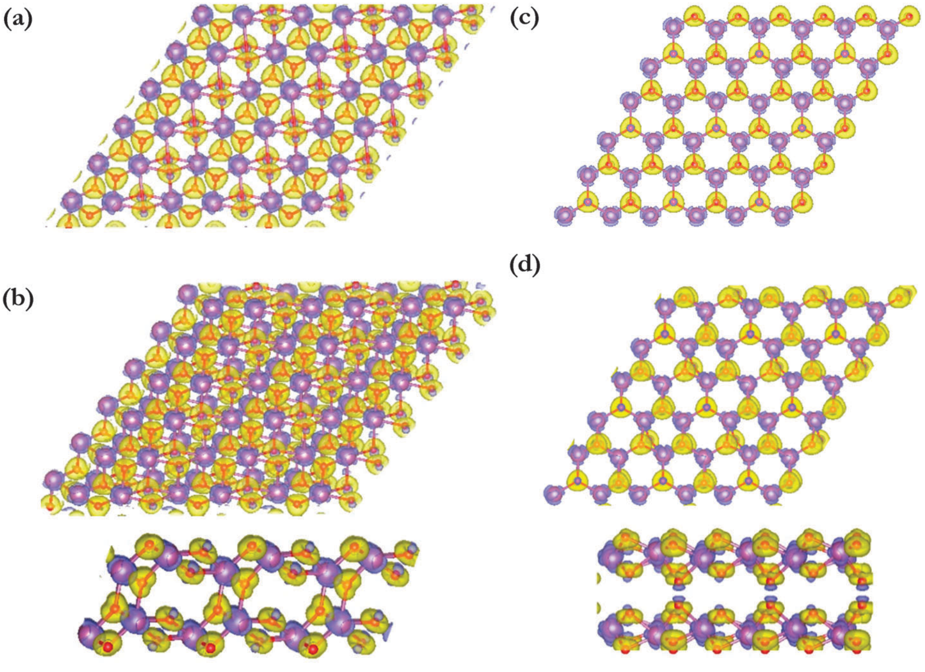

Fig. 2 Top views of the deformation charge density landscape of (a) T-ScO_2 monolayer, (b) T-ScO_2 bilayer, (c) H-ScO_2 monolayer, and (d) H-ScO_2 bilayer. The contour isovalue is 0.02 e Å^{-3}. Yellow: accumulation region; purple: depletion region.

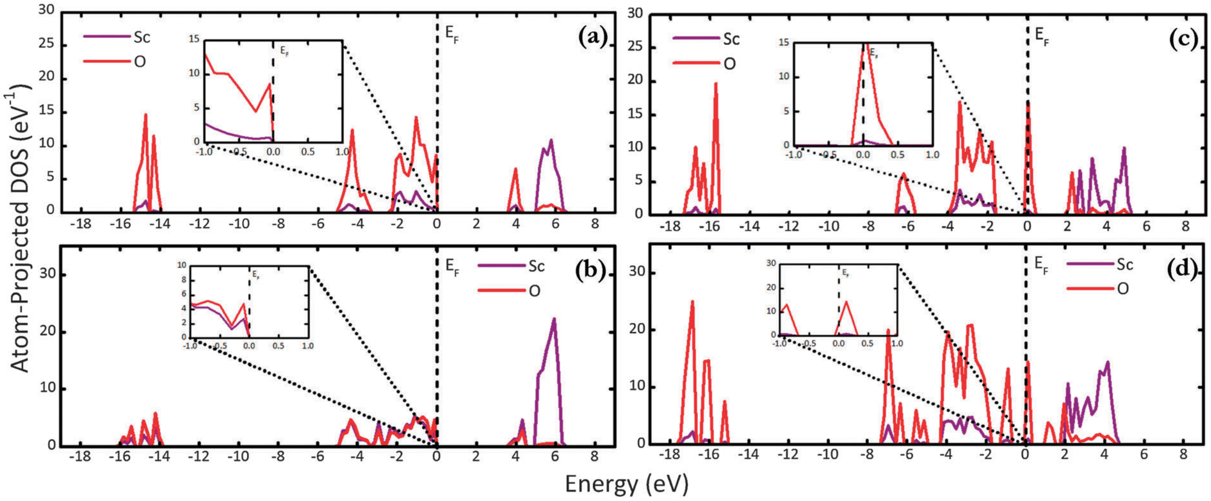

Fig. 3 Atom-projected density of states of (a) T-ScO_2 monolayer, (b) T-ScO_2 bilayer, (c) H-ScO_2 monolayer, and (d) H-ScO_2 bilayer. Zero is taken to be the Fermi energy. The insets show the magnified views of the states near the Fermi level.

are not accounted for. We believe that the disparities in the calculated band gaps can be mainly ascribed to the difference in formalism of the exchange–correlation functional (LDA and LDA + U against GGA + U) in these two studies.

To ascertain the character of states at different k-points, the atom-projected electronic band structures are derived (Fig. S3, ESI†). The occupied and unoccupied bands near the Fermi level including the valence band maximum (VBM) and conduction band minimum (CBM) mainly originate from O atoms. Note that states projected from Sc are degenerate with those from O between −5 and 0 eV in the T-phase, and between −7 and 0 eV in the H-phase (Fig. 3). Due to smaller spectral weights, these Sc bands are obscured behind those contributed by O (Fig. S1, ESI†). The slight lowering of the band gap from the bilayer to the monolayer of the T-phase is in stark contrast to some TMDs; for example, the MoS_2 bilayer has a band gap of 1.53 eV,[68] which is considerably lower than that of its monolayer at 1.80 eV.[69–71] In the T-phase, VBM is shifted from K to M, while CBM remains generally invariant at M. On the other hand, the metallic bands in the H-phase are almost flat along Γ–M–K–Γ. In comparison to the monolayer, additional bands are induced in the valence band of the bilayer at around −1 eV and in the conduction band at around 1 eV.

3.3 Magnetic properties: spin density

To investigate the preferred spin states of ScO_2 in the equilibrium configuration, we consider the material to be in the non-magnetic, ferromagnetic (FM) and antiferromagnetic (AFM) spin configurations. In the non-magnetic state, the spin moment of each atom is initialized to be zero. On the other hand, we define the initial FM spin configuration to consist of parallel (↑↑) spins between all atoms. The initial AFM spin configuration is defined to consist of anti-parallel (↑↓) spins between neighboring atoms of the same sub-layer and between neighboring atoms in the same O–Sc–O unit cell.

The spin-polarized atom-projected density of states is shown in Fig. 4. The T-phase monolayer and bilayer are non-magnetic (Fig. 4(a) and (b)). Occupied states in the vicinity of the Fermi level have energies between −6 and 0 eV. In the H-phase monolayer, two AFM configurations are almost degenerate in energy, with a difference of 0.3 meV – one is converged from the initial FM configuration (hereafter named as AFM_{1st}, Fig. 4(c) inset) and the other is relaxed from the initial AFM configuration (AFM_{2nd}, Fig. 4(d) inset). The spin density distribution of both configurations is similar; at the contour isovalue of 0.01 e Å^{-3}, diagonal rows of O have a net spin density – the regions in grey have a larger spin-up density (*i.e.* $n_{up} - n_{down} > 0$), while those in yellow have a larger spin-down density (*i.e.* $n_{up} - n_{down} < 0$). The total energy of the NM configuration is larger than the AFM configurations by 1.09 eV. The magnetization moment of AFM_{1st} (0.215 μ_B per ScO_2) is greater than that of AFM_{2nd} (0.198 μ_B per ScO_2). In contrast, calculations under the LDA scheme in ref. 25 predict a magnetization moment of 1 μ_B per ScO_2, but it is unclear from that work which type of magnetic ordering the monolayer is in or how the spin density is distributed. Despite the energy degeneracy of AFM_{1st} and AFM_{2nd}, the spin states have different energy levels. The spin-down states in the AFM_{1st} configuration are finite at the Fermi level while the spin-up states have a band gap, *i.e.* the monolayer is half-metallic (Fig. 4(c)). In the AFM_{2nd} configuration, states between −5 and −1 eV experience exchange splitting of approximately 0.7 eV (Fig. 4(d)).

Conversely, the H-phase bilayer remains FM-coupled between neighboring O atoms after relaxation from the initial FM configuration (Fig. 4(e)). The spin density is arranged in alternate diagonal rows of O (Fig. 4(e) inset). In the AFM equilibrium configuration, the spin-up states alternate with spin-down states in diagonal O rows, but the states of the same spin are aligned on top of each other (Fig. 4(f) inset). The FM configuration is degenerate in energy with the AFM configuration, with a small difference of 0.2 meV, while the NM configuration is 0.94 eV greater. The magnetization moment

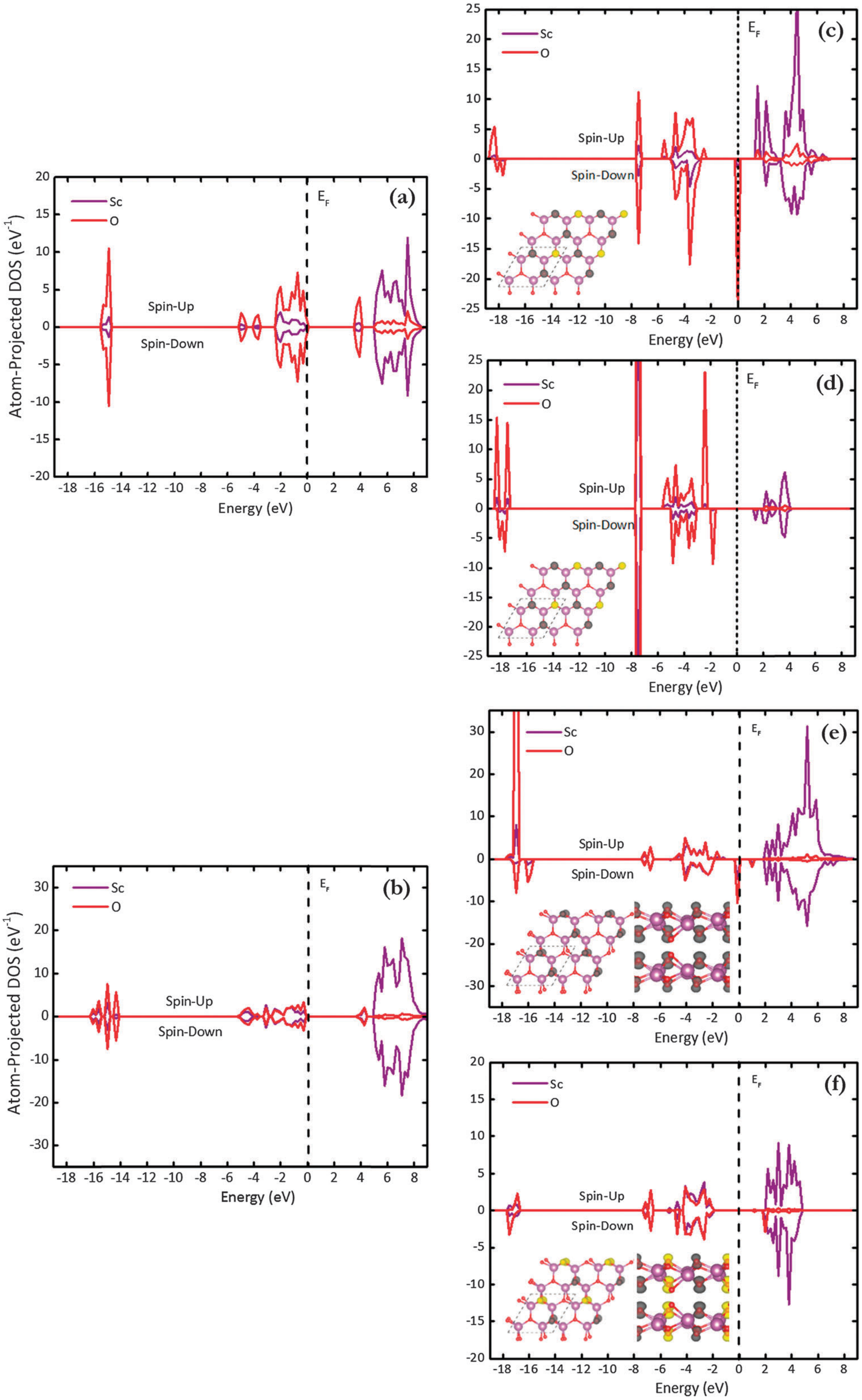

Fig. 4 Spin-polarized atom-projected band structure of (a) T-ScO_2 monolayer, (b) T-ScO_2 bilayer, (c) H-ScO_2 monolayer in the AFM_{1st} configuration, (d) H-ScO_2 monolayer in the AFM_{2nd} configuration, (e) H-ScO_2 bilayer in the FM configuration, and (f) H-ScO_2 bilayer in the AFM configuration. The insets from (c) to (f) illustrate the spin density distribution. The contour isovalue is 0.01 e Å^{-3}. Regions in grey have a net spin-up density, whereas those in yellow have a net spin-down density. Zero is taken to be Fermi energy.

of the FM configuration is 0.225 μ_B per ScO_2 while opposite spins in the AFM configuration nullify to give it zero magnetization moment.

The spin-polarized band structures are then calculated (Fig. 5–7). Spin-up and spin-down bands are degenerate in the nonmagnetic T-phase (Fig. 5). Note that as before, the Sc bands near the Fermi level have a smaller spectral weight than those from O and are therefore concealed behind the O bands. In the T-phase monolayer, at an isovalue of 0.01 e $Å^{-3}$, states at CBM (as denoted by the green circle in Fig. 5(a)) are localized at O atoms between the Sc zigzag rows, whereas those at VBM (blue circle) are distributed around O atoms within the zigzag rows. Careful observation of the spatial character of the orbitals and the orientation of these states with respect to the axes uncovers the nature of these states. They match closely to p-orbitals with 1 angular node and 2 large lobes; they have a dominant p_y and p_z character as the lobes are aligned in the y–z plane. Similarly, the states at CBM in the T-phase bilayer are located at O atoms between Sc rows and are predominantly p_y and p_z in shape and orientation (Fig. 5(b)). However, in comparison to those in the monolayer, they are evenly distributed in neighboring O atoms, while in the monolayer, the localization of the states alternates between neighboring O atoms. The states at VBM in the bilayer resemble those in the monolayer; they are mainly located around O atoms within the Sc zigzag rows.

In AFM_{1st} of the H-phase monolayer, the top of the spin-up valence band is almost flat and VBM is located at K. Similarly, the bottom of the spin-up conduction band is nearly flat and CBM is at Γ. At an isovalue of 0.01 e $Å^{-3}$, the states at VBM and CBM are evenly distributed around alternating O atoms (Fig. 6(a)). On the other hand, the spin-down states are metallic with a bandwidth of 0.25 eV. In AFM_{2nd}, the metallic spin-down states have a smaller bandwidth of approximately 0.20 eV, as

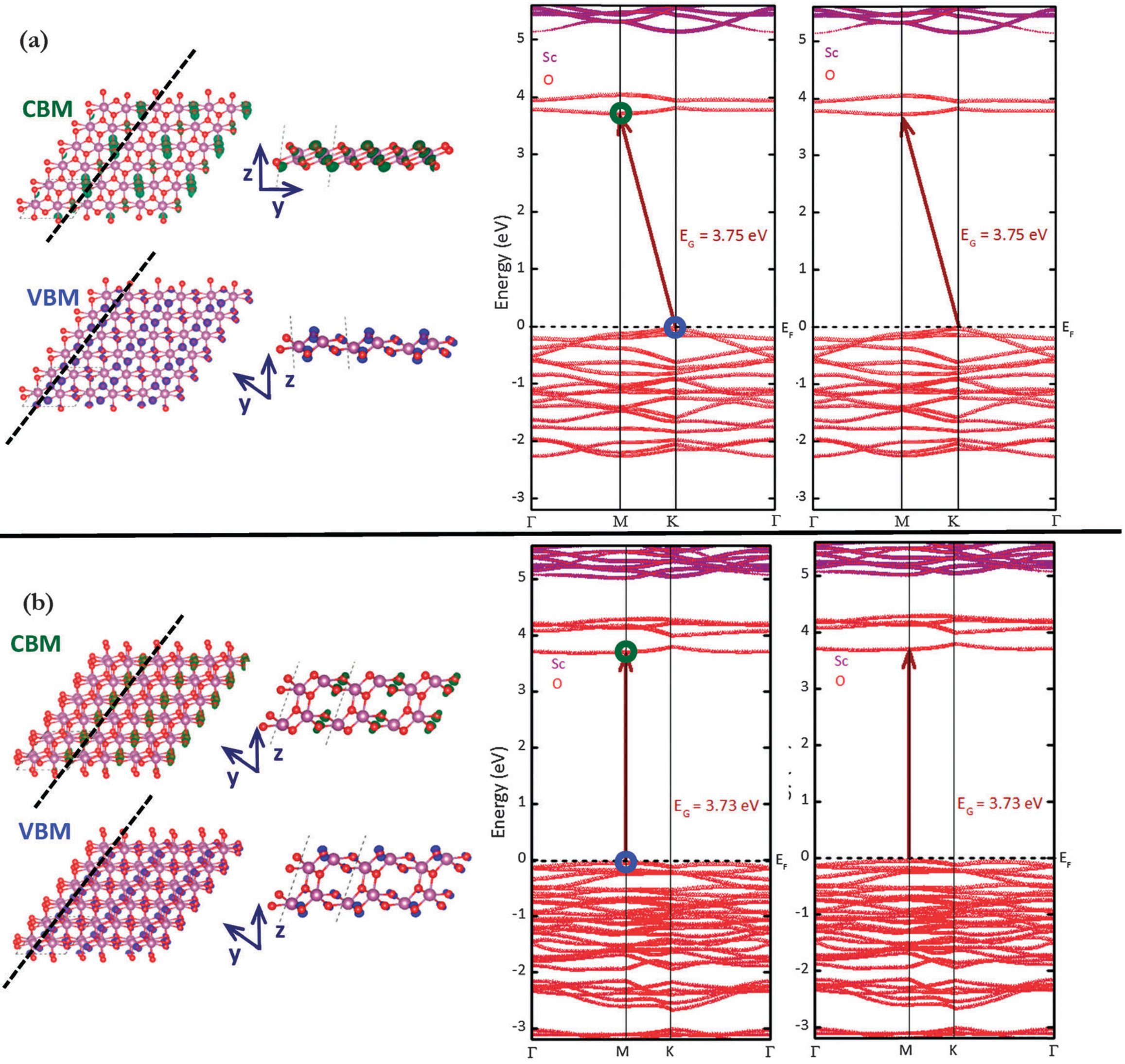

Fig. 5 (a) T-ScO_2 monolayer, (b) T-ScO_2 bilayer. For each panel, top views, side views of the partial charge density landscape at CBM and VBM, and spin-polarized atom-projected density of states are shown. The size of the data points indicates the spectral weight. Zero is taken to be Fermi energy.

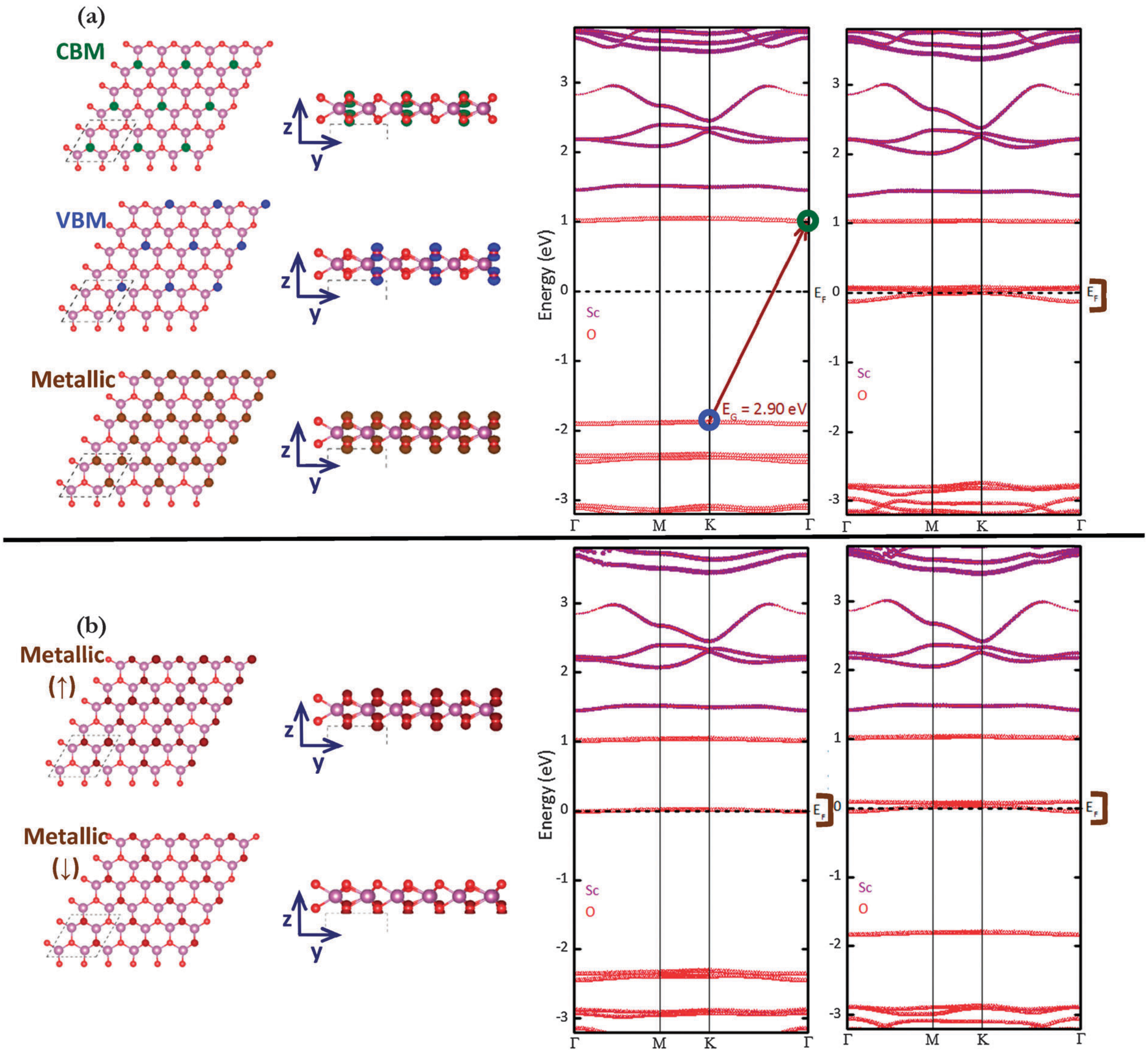

Fig. 6 (a) AFM_{1st} and (b) AFM_{2nd} spin configurations of H-ScO_2 monolayer. For each panel, top views and side views of the partial charge density landscape at CBM and VBM, of the metallic states, and spin-polarized atom-projected density of states are shown. The size of the data points indicates the spectral weight. Zero is taken to be Fermi energy.

compared to 0.10 eV for the spin-up states (Fig. 6(b)). Note that the states near the Fermi level are not discernible in Fig. 4(d), but are evident in Fig. 6(b). Unlike the spin-up states which are distributed in both O sublayers, the spin-down states are localized only around O atoms in the lower sub-layer. All states at VBM and CBM with the isovalue of 0.01 e $Å^{-3}$ have a prevalent p_z-character.

In the FM configuration of the H-phase bilayer, the spin-up states have a larger band gap than that of the spin-down states (Γ–Γ: 2.07 and 1.11 eV, Fig. 7(a)). The localization of the CBM states at alternating diagonal rows of O is similar to that in the monolayer (Fig. 6(a)). States at VBM are more densely distributed in the bilayer. In the AFM configuration, the transition from VBM to CBM is indirect from K to Γ. As before, the O-p_z states dominate the top of the valence band and the bottom of the conduction band.

Due to strong Coulomb interactions between Sc-3d and O-2p orbitals, one would expect them to dictate the electronic structure of the material. To verify this, the spin-polarized band structures are projected onto Sc-d and O-p orbitals to gain an insight into the contribution of each orbital (Fig. S4–S7, ESI†). In the case of the H-phase, only the half-metallic monolayer (AFM_{1st}) and the FM-coupled bilayer are shown and discussed for the sake of brevity. The color and size of the data points are assigned in correspondence with its relative spectral weight; those with larger weight are in red. For all configurations, the top of the valence band and the bottom of the conduction band are mainly contributed by O-p_y, and particularly O-p_z states. Comparison between the band structures of the T- and H-phases shows that the metallic character of the H-phase originates from Sc-d_{yz}, Sc-d_{xz}, and O-p_z orbitals. In a similar vein, exchange splitting of the states of the H-phase in both

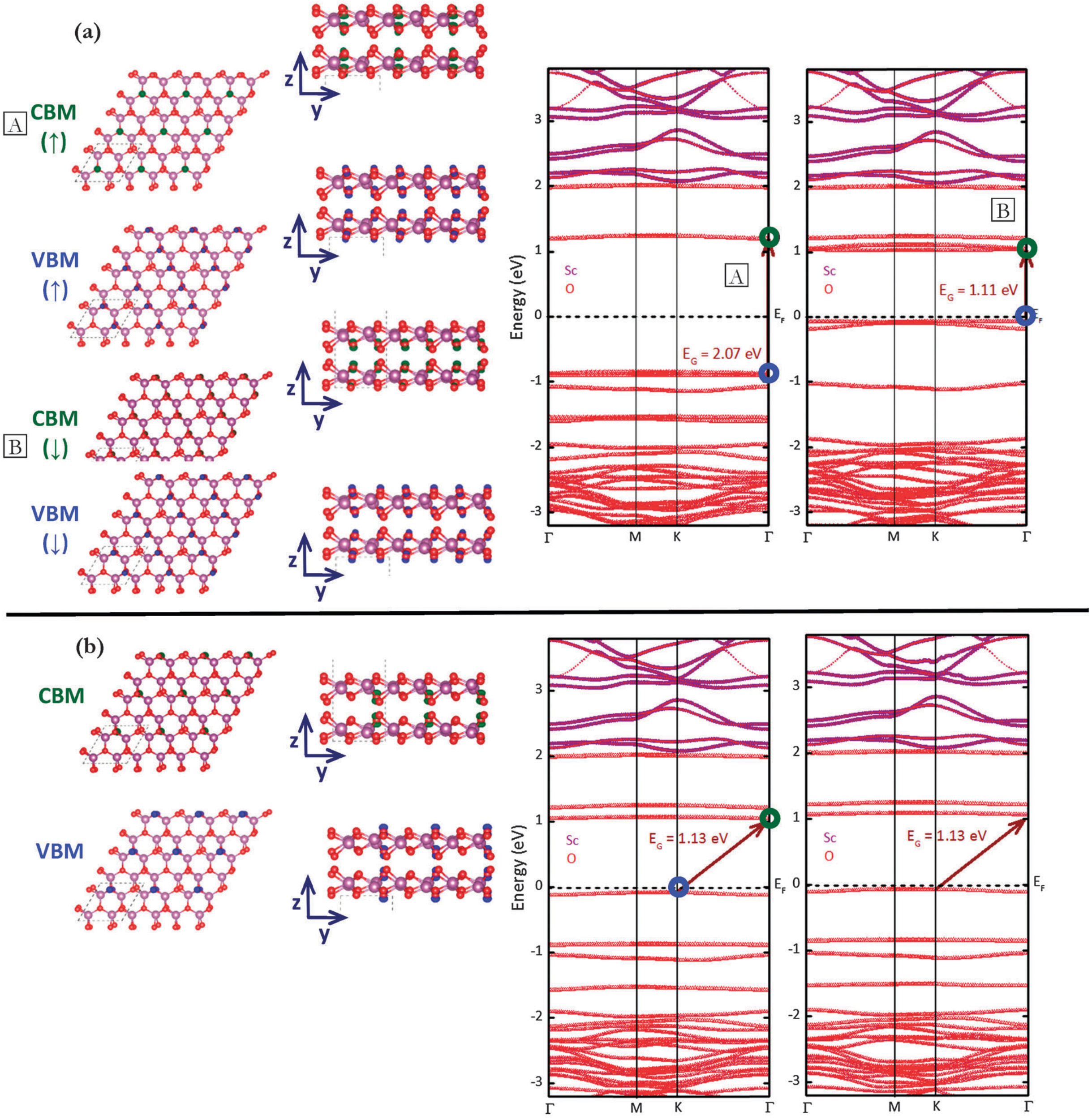

Fig. 7 (a) FM and (b) AFM spin configurations of H-ScO_2 bilayer. For each panel, top views and side views of the partial charge density landscape at CBM and VBM, of the metallic states, and spin-polarized atom-projected density of states are shown. The size of the data points indicates the spectral weight. Zero is taken to be Fermi energy. A and B differentiate between CBM and VBM of spin-up and spin-down states.

spins is most evident for O-p_z (Fig. S6 and S7, ESI†). Succinctly, O-p_z states play a critical role in the electronic and magnetic properties of T- and H-ScO_2.

3.4 Chemical bonding

The electronic structure of a material is inherently associated with the nature of its bonds. In this regard, to gain a more complete outlook of the electronic properties of ScO_2, we analyse its chemical bonding. A chemical bond, or more specifically, the electron density distribution between atoms can be described accurately by a few tools – two of which are the Laplacian of the electron density *via* the quantum theory of atoms in molecules,[72–77] and the Born effective charge tensor (Z^*).[78] Further explanation of the Laplacian is given in the ESI.†

In general, the covalency of the bonds is expressed by (1) the form of the zero envelope of the negative Laplacian and (2) the value of the negative Laplacian at the bcp. The left panels of Fig. 8 show the 2D and 3D negative Laplacian ($-\nabla^2\rho$) plots of Sc–O pairs in different configurations, as illustrated by the shaded regions in Fig. 1. The grey dots represent the bcp in the charge profile and the lines radiating from each atom denote the gradient vector field lines of charge density. The blue bold line is the zero envelope, whereas the red and green lines are contour lines with a value of -5 and -10 e Å^{-5}, respectively.

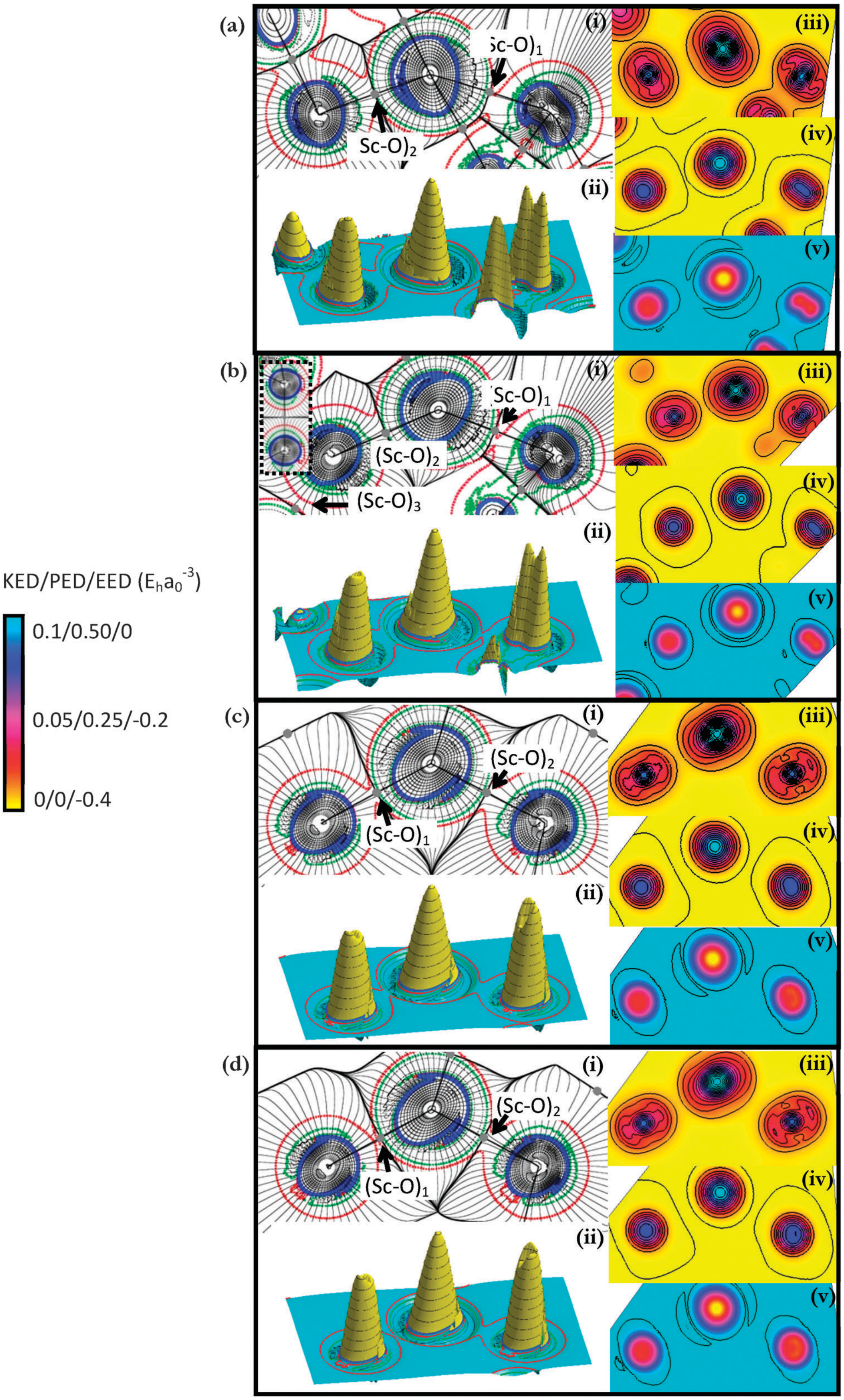

Fig. 8 (a) T-ScO_2 monolayer, (b) T-ScO_2 bilayer, (c) H-ScO_2 monolayer, and (d) H-ScO_2 bilayer: (i) 2D negative Laplacian plot, (ii) 3D negative Laplacian plot, (iii) kinetic energy density, (iv) potential energy density, and (v) electronic energy density. The color bar shows the energy density in $E_h a_0^{-3}$, whereby E_h is Hartree and a_0 is Bohr radius.

In all configurations, none of the zero envelopes enclose the Sc–O bcp, indicating that the Sc–O bonds are more ionic than covalent. In the T-phase monolayer (Fig. 8(a)), $-\nabla^2\rho$ at the bcp $(\text{Sc–O})_1$ and $(\text{Sc–O})_2$ are −7 and −10 e Å^{-5}, respectively, whereas ρ is 0.55 e Å^{-3} at both points. This suggests that the two Sc–O bonds, which are not of equal length (Fig. 1(a)), are slightly ionic and do not have the same covalency. The intralayer Sc–O bonds in the T-phase bilayer (Fig. 8(b)) have a similar $-\nabla^2\rho$ at the bcp [$(\text{Sc–O})_1$: −7; $(\text{Sc–O})_2$: −10 e Å^{-5}], while ρ are slightly smaller at 0.35 and 0.50 e Å^{-3}, respectively. $(\text{Sc–O})_3$ is a pair of interlayer atoms and $-\nabla^2\rho@(\text{Sc–O})_3 = -7$ and $\rho@(\text{Sc–O})_3 = 0.35$. The bcp between the layers and its finite value of ρ validates the presence of bonds between the layers. Note that the grey region, shown in Fig. 1(b), illustrates the 2 Sc and 2 O atoms in $(\text{Sc–O})_1$, $(\text{Sc–O})_2$, and $(\text{Sc–O})_3$, and the inset in Fig. 8(b) shows the topology for the same $(\text{Sc–O})_3$ pair, but is taking a different 2D plane from that in the main figure. In general, the covalency of bonds is dictated by both the Laplacian value and the charge density at the bcp; a bond with a lower ρ at its bcp is more ionic than the other, if their Laplacian values are equivalent. However, this is not a hard and fast rule. In our context, the slightly lower charge density at the bcp of $(\text{Sc–O})_1$ and $(\text{Sc–O})_2$ relative to that of the monolayer is attributed to the sharing of electrons between intra- and interlayer Sc–O bonds.

In the H-phase monolayer (Fig. 8(c)) and bilayer (Fig. 8(d)), $-\nabla^2\rho@(\text{Sc–O})_1 = -8$, $-\nabla^2\rho@(\text{Sc–O})_2 = -8$, while ρ is 0.55 e Å^{-3} in the former and 0.35 e Å^{-3} in the latter. Akin to the T-phase, electron sharing between intra- and interlayer bonds reduces the charge density at the bcp in the bilayer. The two bcp within each H-phase structure have the same $-\nabla^2\rho$ and ρ, *i.e.* they have the same chemical topology. In contrast to that in the T-phase (Fig. 1), the uniform chemical topology in the H-phase correlates well with its relatively small variation of bond lengths.

Presented in the right panels are the kinetic energy density (KED) (iii), potential energy density (PED) (iv), and electronic energy density (EED) (v) of the same 2D plane. The EED is the sum of KED and PED, and it complements the $-\nabla^2\rho$ plot; it is more negative if the bond has a greater covalent character. The EED at all bcp are in cyan on the color bar. This corresponds to a value close to null and again verifies the highly ionic nature of the Sc–O bonds.

QTAIM provides a graphical depiction of the charge distribution from which the covalency of the bonds can be deduced. Conversely, Born effective charges (BEC), or transverse charges, Z^*, establish the covalency of the bonds in a macroscopic manner; it is a proportionality coefficient relating the change in polarization in the direction β and the displacement of an ion i in the direction α in the absence of an external electric field,

$$Z_{i\alpha\beta}{}^* = \Omega \frac{\Delta P_\beta}{\Delta u_{i\alpha}}\bigg|_{\varepsilon=0} \tag{4}$$

It describes the linear relation between the force acting on an atom and the macroscopic electric field[78–80] and hence governs the amplitude of long-range Coulomb interaction between ions. It is this interaction that causes the splitting between transverse and longitudinal optic (LO) and transverse optic (TO) phonon modes.[78–80] From another point of view, it can also be represented as the macroscopic current flowing through the material as a particular ion is adiabatically displaced, while all other ions are kept fixed. In a closed shell system, the charge carried by an ion will be close to its formal valence. On the other hand, if the bonds have a covalent character, a significant amount of charge flows through it when ions are displaced, and therefore, the deviation of Z^* from the formal charge is large.[81,82]

In a non-cubic lattice, the diagonal elements of the Born effective charge tensor are non-identical, *i.e.* the charges are anisotropic. Indeed, for each configuration of this study, the diagonal elements of Z^* are dissimilar due to the asymmetry of the structure (Table 1). In a closed shell system, the formal valence of Sc, and O in ScO_2 are 3+ and 2−, respectively. As $Z_{xx}{}^*$ and $Z_{yy}{}^*$ for the H-phase monolayer deviate less with respect to their formal valence, relative to corresponding tensor components in the other 3 structures, its Sc–O bonds are more ionic than those in other configurations. In this way, the Born effective charge analysis supplements the QTAIM analysis by 'quantifying' the covalency of the Sc–O in each configuration.

3.5 Unique response of electronic properties to strain on ScO_2 bilayer

Fig. 2 has shown that charges are transferred between layers in a ScO_2 bilayer; the bcp between the layers in the QTAIM analysis (Fig. 8) further justifies the bond formation between layers. This suggests that interaction between layers is key to the electronic behavior of the ScO_2 bilayer. One way to evaluate this interaction strength and to examine the effects of the additional layer on the electronic and magnetic properties of

Table 1 Matrix components of the Born effective charge tensor Z^* of T-ScO_2 monolayer, T-ScO_2 bilayer, H-ScO_2 monolayer, and H-ScO_2 bilayer

		Born effective charge tensor (Z^*)								
		xx	*yy*	*zz*	*xy*	*xz*	*yx*	*yz*	*zx*	*zy*
T-ScO_2 monolayer	Sc	3.970	3.702	0.931	0.284	−0.078	0.293	0.428	0.007	0.185
	O	−1.990	−1.855	−0.467	−0.142	0.039	−0.146	−0.214	−0.004	−0.092
T-ScO_2 bilayer	Sc	3.800	3.645	0.427	0.271	0.248	0.293	0.155	0.362	−0.130
	O	−1.903	−1.828	−0.579	−0.135	−0.124	−0.146	−0.077	−0.160	0.054
H-ScO_2 monolayer	Sc	3.298	3.009	0.606	−0.300	0	−0.204	0	0	0
	O	−1.686	−1.524	−0.304	0.148	0	0.104	0	0	0
H-ScO_2 bilayer	Sc	3.507	3.699	0.824	−0.177	0	−0.176	0	0	0
	O	−1.759	−1.864	−0.227	0.089	0	0.088	0	0	0

the material is to apply strain in the direction normal to its surface. In other words, the layers are compressed towards or pulled away from each other.

The interlayer separation is varied from 1.57 to 3.77 Å for the T-phase and from 1.77 to 3.97 Å for the H-phase, spanning from the compressive to the tensile regime (Fig. 9). The band gap of the T-phase decreases from 3.73 eV at the ground state to 3.57 eV at a separation of 1.57 Å. A small tensile strain induces an increase in the band gap to the maximum value of 4.01 eV at an approximate separation of 3.00 Å ①. Note that the change in the band gap from 3.57 to 4.01 eV is more than 10%. For the H-phase, a compressive strain (1.97 to 1.77 Å) opens up a band gap (E_g = 21 meV). Similarly, a small tensile strain ① induces a band gap (E_g = 11 meV), but increasing the strain beyond that, the band gap reduces and eventually vanishes at a separation of around 2.97 Å ②. Together with the band gap, the formation energy of each structure, as calculated using eqn (1), is presented. The H-phase is predicted to be more stable (with a darker red in the color bar) than its ground state when the layers are separated by more than 2.97 Å, while the H-phase metallic structures are generally more stable than the semiconducting ones. The T-phase bilayer is more stable than its H-phase counterpart within the range of interlayer separation studied.

Apart from the unique electronic behavior, the H-phase bilayer also exhibits interesting spin characteristics with the application of strain. Fig. S8 (ESI†) shows the spin density distribution at three different interlayer separation values. For the FM configuration (refer to Fig. 7) at a separation of 1.77 Å, the material is compressively strained. Domains of spin-up states are located in alternating diagonal rows of O. As the separation is increased towards the ground state configuration, the spin density distribution remains unchanged. At the ground state, additional smaller domains of spin-up states emerge. The distribution remains constant as the separation is increased to 3.97 Å. However, at infinite separation, *i.e.* a monolayer, it becomes AFM-coupled across diagonal layers. A similar behavior is observed for the AFM configuration in the bilayer.

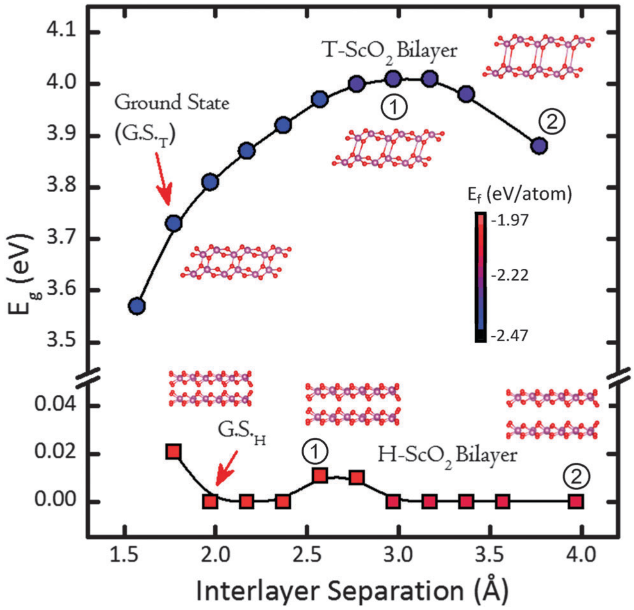

Fig. 9 Variation of the band gap (E_g) with the interlayer separation in T-ScO$_2$ and H-ScO$_2$ bilayers. Atomic configurations are shown: at the ground state (G.S.), at the maxima of the band gap and the largest interlayer separation investigated in the study. The data points are colour-coded to denote the formation energy.

Why do the two phases differ so much in their response to strain? It is even more compelling in the H-phase bilayer since it transforms from a metal to a semiconductor and back to a metal as the tensile strain applied is increased in magnitude. As O-p$_z$ states dominate the top and bottom of the valence and conduction bands, respectively, the effects of varying the interlayer separation on the O-p$_z$ bands are investigated (Fig. 10 and 11). By charting the evolution of the O-p$_z$ bands with the interlayer separation, the unique response of the bilayers to strain, as observed in Fig. 10, can then be perused.

In Fig. 10(a), 6 bands, namely, A–D in the conduction band and E and F in the valence band of the T-phase bilayer, have been highlighted in the leftmost panel to draw attention to their trend of change with the separation between layers. In the conduction band, band A (in yellow) shifts to higher energies from an interlayer separation of 1.57 Å to 2.97 Å, beyond which it moves downwards slightly to a lower energy (Fig. 10(a) and (b)). Bands B–D (B: green; C: blue; D: grey) generally follow the same trend, but reach a maximum energy at a smaller separation of either 2.17 Å or 2.57 Å (Fig. 10(b)). Bands B and D (and bands A and C) approach each other as the separation increases. On the other hand, the shift of bands E and F in the valence band to higher energies with the separation is less significant since other bands are present around the VBM. The plots in Fig. 10(b) are then extrapolated to infinite separation, *i.e.* a T-phase monolayer. The last few panels of Fig. 10(a) show the consistent trend of bands A–D as they shift downwards in energy towards the Fermi level; eventually bands B:D, A:C, and E:F merge to become degenerate. All in all, the increase and then decrease of the band gap with the interlayer separation is chiefly due to the shift of the lowest unfilled O-p$_z$ band. Moreover, the band evolution from a bilayer to a monolayer unveils the degenerate nature of the O-p$_z$ bands near the Fermi level.

The band structure of the H-phase bilayer responds in a distinctly different manner from that of the T-phase bilayer. 2 bands near the Fermi level are marked in Fig. 11 to facilitate tracking of the transformation. Band A in the valence band is almost flat at the ground state. With the application of tensile strain, it shifts upwards towards the Fermi level, and bends in a way such that the energy levels around M and K are higher than that around Γ. It eventually crosses the Fermi level at M and K when the separation is increased to 3.17 Å. Band B in the conduction band cuts the Fermi level near Γ. Increasing the separation further to 3.57 Å lifts the band slightly above the Fermi level. At an infinite separation (*i.e.* monolayer), band A is shifted to about 0.05 V below the Fermi level while band B crosses the Fermi level again near Γ. Therefore, the metallic

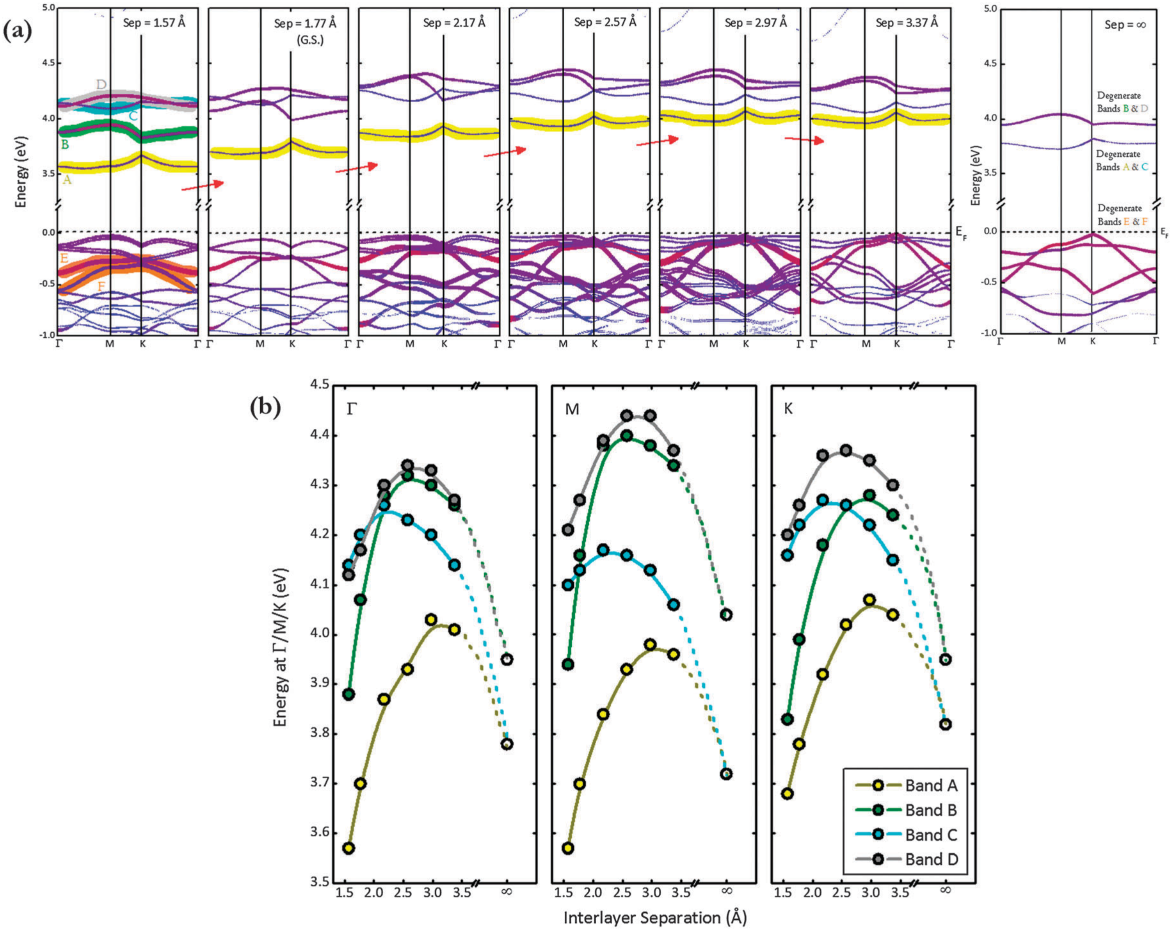

Fig. 10 (a) Evolution of O-p_z states with the interlayer separation in T-ScO$_2$ bilayer. The O-p_z states in T-ScO$_2$ monolayer is used as a reference in the last panel. Bands A–F are highlighted for clarity. (b) Variation of the energy at *Γ*, *M*, and *K* for bands A–D in T-ScO$_2$ bilayer.

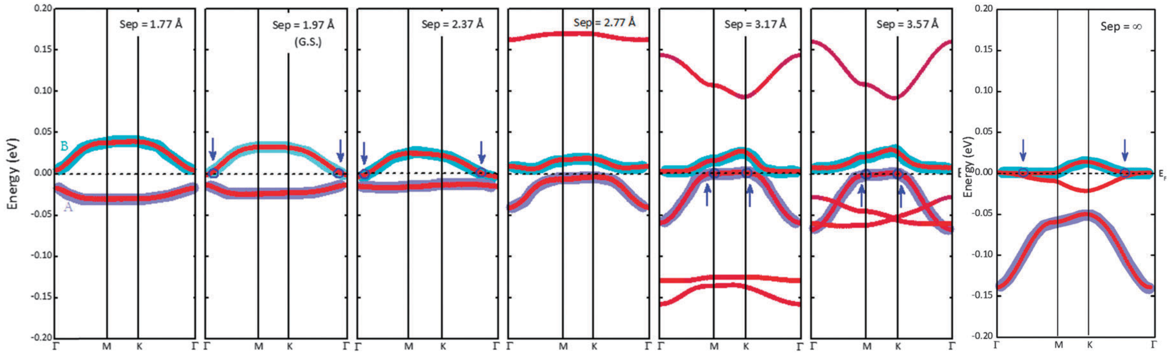

Fig. 11 Evolution of O-p_z states with the interlayer separation in H-ScO$_2$ bilayer. The O-p_z states in T-ScO$_2$ monolayer is used as a reference in the last panel. Bands A and B are highlighted for clarity. The blue arrows mark the points at which the Fermi level is crossed.

character near the ground state, and with tensile strain, stems from the crossing of a different band at the Fermi level. The shape transformation of bands close to the Fermi level with the interlayer separation induces the metal → semiconductor → metal transition.

Unlike the bands in T-phase bilayers, bands A and B of H-phase bilayers evolve in shape with the interlayer separation. This transformation can be characterized by the gradient of the bands with respect to the wavevector, also known as the Fermi velocity.

$$v_F = \frac{E}{\hbar k} \tag{4}$$

where $\hbar$ is the reduced Planck constant.

Fig. 12 shows the variation of Fermi velocity of bands A and B with the separation. The red circles mark the velocity of the

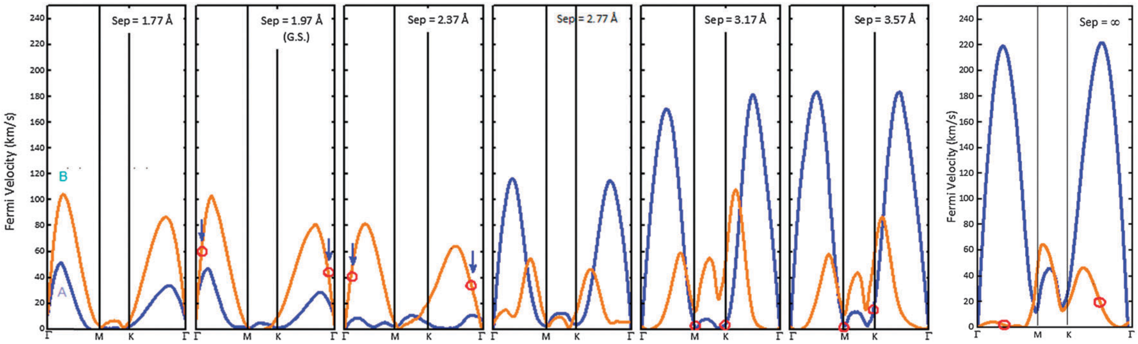

Fig. 12 Evolution of the Fermi velocity of bands A and B with the interlayer separation in H-ScO_2 bilayer. The Fermi velocity of the same bands in T-ScO_2 monolayer is used as a reference in the last panel. The red circles mark the Fermi velocity of the metallic states.

metallic states, with reference to Fig. 11. At the ground state, the Fermi velocity of the metallic states (band B) is approximately 60 km s^{-1} at ΓM and 40 km s^{-1} at ΓK. At a larger separation of 2.37 Å, the Fermi velocity of these states decreases to less than 40 km s^{-1}. Increasing the separation further reduces the Fermi velocity of the metallic states to almost zero before it becomes larger in its evolution towards a monolayer.

4. Summary

Transition metal oxides (TMOs) are a family of materials in which Coulomb interactions between certain electrons is significantly stronger than in typical materials. Due to strong correlation effects, these materials exhibit an array of unique properties. One such TMO in the 2D MX_2 configuration is ScO_2. A previous study,[25] which has performed first-principles calculations using the LDA/LDA + U scheme, has predicted that T- and H-ScO_2 monolayers are stable. In this study, we extend the investigation to the ScO_2 bilayer under the generalized-gradient approximation with on-site Coulomb interaction (GGA + U); the geometry, energetics, electronic properties, magnetic properties, and chemical bonding (analyzed by QTAIM and the Born effective charge tensor) of the (i) T-phase monolayer, (ii) T-phase monolayer, (iii) H-phase monolayer, and (iv) H-phase bilayer are examined. Their properties are presented as follow:

(1) Interlayer bonding: In the presence of strong correlation effects, charges are transferred on atoms between layers in ScO_2 bilayers, *i.e.* atoms between layers are bonded. However, the closest neighbor pairs are different in the two phases; in the T-phase bilayer, these pairs are Sc–O, while in the H-phase bilayer, they are O–O.

(2) Electronic properties: The T-phase monolayer and bilayer are wide-band gap semiconductors with band gaps of 3.75 and 3.73 eV, respectively. The metallicity of the H-phase monolayer and bilayer originates from the Sc-d_{yz}, Sc-d_{xz}, and O-p_z orbitals.

(3) Magnetic properties: The T-phase is non-magnetic. The H-phase monolayer has two energy-degenerate AFM spin configurations: the first of which has a magnetization moment of 0.215 μ_B per ScO_2 and the second has a moment of 0.198 μ_B per ScO_2. The FM configuration (0.225 μ_B per ScO_2) of the H-phase bilayer is degenerate with its AFM configuration (0 μ_B per ScO_2). Exchange splitting is most significant for O-p_z states in the H-phase.

(4) Chemical bonding: The Sc–O bonds are highly ionic. In comparison to other configurations, the chemical topology in the H-phase monolayer is relatively more uniform, and its bonds are more ionic. The interlayer bcp in the bilayers and its finite value of ρ validates the presence of bonds between the layers shown in the deformation charge density plots.

The interaction strength between layers in the bilayers is examined by applying strain in the direction normal to the material surface. Interestingly, the two phases respond in a distinctly dissimilar manner; the band gap of the T-phase bilayer increases with tensile strain before it decreases, with a variation of more than 10%, while the T-phase bilayer becomes a semiconductor and then becomes a metal with the increase of tensile strain. The mechanism for such a response is – T-phase bilayer: shift of the lowest unfilled O-p_z band; H-phase bilayer: shape transformation of bands close to the Fermi level. The Fermi velocity of the metallic states in the H-phase bilayer decreases with the interlayer separation before increasing slightly towards the monolayer.

By employing the GGA + U formalism, the present study examines the electronic properties of ScO_2 from a different perspective. The interaction between layers allows tailoring of the electronic properties in the direction normal to the material surface. The versatility of adjusting the electronic behavior of ScO_2 can be valuable to the development of next-generation nanodevices.

Conflicts of interest

The authors declare no competing financial interest.

Acknowledgements

G.C.L. gratefully acknowledges A*STAR for funding under the A*STAR International Fellowship (2013–2015). The computations were performed on the MTU Superior cluster, and support from Dr S. Gowtham is appreciated.

References

1 K. S. Novoselov, A. K. Geim, S. V. Morozov, D. Jiang, Y. Zhang, S. V. Dubonos, I. V. Grigorieva and A. A. Firsov, Electric field effect in atomistically thin carbon films, *Science*, 2004, **306**, 666–669.

2 K. S. Novoselov, A. K. Geim, S. V. Morozov, D. Jiang, M. I. Katsnelson, I. V. Grigorieva, S. V. Dubonos and A. A. Firsov, Two-dimensional gas of massless dirac fermions in graphene, *Nature*, 2005, **438**, 197–200.

3 C. L. Kane and E. J. Mele, Quantum spin Hall effect in graphene, *Phys. Rev. Lett.*, 2005, **95**, 226801.

4 M. I. Katsnelson, K. S. Novoselov and A. K. Geim, Chiral tunnelling and the Klein paradox in graphene, *Nat. Phys.*, 2006, **2**, 620–625.

5 M. I. Katsnelson, Zitterbewegung, chirality, and minimal conductivity in graphene, *Eur. Phys. J. B*, 2006, **51**, 157–160.

6 C. W. J. Beenakker, Specular Andreev reflection in graphene, *Phys. Rev. Lett.*, 2006, **97**, 067007.

7 A. K. Geim and K. S. Novoselov, The rise of graphene, *Nat. Mater.*, 2007, **6**, 183–191.

8 C.-K. Chang, S. Kataria, C.-C. Kuo, A. Ganguly, B.-Y. Wang, J.-Y. Hwang, K.-J. Huang, W.-H. Yang, S.-B. Wang and C.-H. Chuang, Band gap engineering of chemical vapor deposited graphene by *in situ* BN doping, *ACS Nano*, 2013, **7**, 1333–1341.

9 K. F. Mak, C. H. Lui, J. Shan and T. F. Heinz, Observation of an electric-field-induced band gap in bilayer graphene by infrared spectroscopy, *Phys. Rev. Lett.*, 2009, **102**, 256405.

10 Y.-W. Son, M. L. Cohen and S. G. Louie, Energy gaps in graphene nanoribbons, *Phys. Rev. Lett.*, 2006, **97**, 216803.

11 C. Chung, Y.-K. Kim, D. Shin, S.-R. Ryoo, B. H. Hong and D.-H. Min, Biomedical applications of graphene and graphene oxide, *Acc. Chem. Res.*, 2013, **46**, 2211–2224.

12 N. Mahmood, C. Zhang, H. Yin and Y. Hou, Graphene-based nanocomposites for energy storage and conversion in lithium batteries, supercapacitors and fuel cells, *J. Mater. Chem. A*, 2014, **2**, 15–32.

13 P. Avouris and C. Dimitrakopoulos, Graphene: synthesis and applications, *Mater. Today*, 2012, **15**, 86–97.

14 Y. Zhu, D. K. James and J. M. Tour, New routes to graphene, graphene oxide and their related applications, *Adv. Mater.*, 2012, **24**, 4924–4955.

15 H. Wang, X. Wang, X. Li and H. Dai, Chemical self-assembly of graphene sheets, *Nano Res.*, 2009, **2**, 336–342.

16 A. Ismach, C. Druzgalski, S. Penwell, M. Zheng, A. Javey, J. Bokor and Y. Zhang, Direct chemical vapor deposition of graphene on dielectric surfaces, *Nano Lett.*, 2010, **10**, 1542–1548.

17 J. P. G. Farr, Molybdenum-disulfide in lubrication – review, *Wear*, 1975, **35**, 1–22.

18 B. W. H. Baugher, H. O. H. Churchill, Y. Yang and P. Jarillo-Herroro, Intrinsic electronic transport properties of high-quality monolayer and bilayer MoS_2, *Nano Lett.*, 2013, **13**, 4212–4216.

19 D. Lembke and A. Kis, Breakdown of high-performance monolayer MoS_2 transistors, *ACS Nano*, 2012, **6**, 10070–10075.

20 D. Braga, I. Gutiérrez Lezama, H. Berger and A. F. Morpurgo, Quantitative determination of the band gap of WS_2 with ambipolar ionic liquid-gated transistors, *Nano Lett.*, 2012, **12**, 5218–5223.

21 M. Chhowalla, H. S. Shin, G. Eda, L. J. Li, K. P. Loh and H. Zhang, The chemistry of two-dimensional layered transition metal dichalcogenide nanosheets, *Nat. Chem.*, 2013, **5**, 263–275.

22 P. Darancet, A. J. Millis and C. A. Marianetti, Three-dimensional metallic and two-dimensional insulating behavior in octahedral tantalum dichalcogenides, *Phys. Rev. B: Condens. Matter Mater. Phys.*, 2014, **90**, 045134.

23 F. Li, K. Tu and Z. Chen, Versatile electronic properties of VSe_2 bulk, few-layers, monolayer, nanoribbons, and nanotubes: a computational exploration, *J. Phys. Chem. C*, 2014, **118**, 21264–21274.

24 Y. Jing, Z. Zhou, C. R. Cabrera and Z. Chen, Metallic VS_2 monolayer: a promising 2D anode material for lithium ion batteries, *J. Phys. Chem. C*, 2013, **117**, 25409–25413.

25 C. Ataca, H. Şahin and S. Ciraci, Stable, single-layer MX_2 transition-metal oxides and dichalcogenides in a honeycomb-like structure, *J. Phys. Chem. C*, 2012, **116**, 8983–8999.

26 B. Lake, G. Aeppli, K. N. Clausen, D. F. McMorrow, K. Lefmann, N. E. Hussey, N. Mangkorntong, M. Nohara, H. Takagi and T. E. Mason, *et al.*, Spins in the vortices of a high-temperature superconductor, *Science*, 2002, **291**, 1759–1762.

27 C. Rossel, K. N. Yang, M. B. Maple, Z. Fisk, E. Zirngiebl and J. D. Thompson, Strong electronic correlations in a new class of Yb-based compounds: $YbXCu_4$ (X = Au, Au, Pd), *Phys. Rev. B: Condens. Matter Mater. Phys.*, 1987, **35**, 1914.

28 M. Miyauchi, A. Nakajima, A. Fujishima, K. Hashimoto and T. Watanabe, Photoinduced surface reactions on TiO_2 and $SrTiO_3$ films: photocatalytic oxidation and photoinduced hydrophilicity, *Chem. Mater.*, 2000, **12**, 3–5.

29 J. C. Slater, *Quantum theory of atomic structure*, McGraw-Hill, New York, 1960.

30 M. Jourdan, J. Minár, J. Braun, A. Kronenberg, S. Chadov, B. Balke, A. Gloskovskii, M. Kolbe, H. J. Elmers and G. Schönhense, *et al.*, Direct observation of half-metallicity in the Heusler compound Co_2MnSi, *Nat. Commun.*, 2014, **5**, 3974.

31 E. Dagotto, Complexity in strongly correlated electronic systems, *Science*, 2005, **309**, 257–262.

32 Y. Tokura and N. Nagaosa, Orbital physics in transition-metal oxides, *Science*, 2000, **288**, 462–468.

33 D. I. Khomskii, Multiferroics: different ways to combine magnetism and ferroelectricity, *J. Magn. Magn. Mater.*, 2006, **306**, 1.

34 R. M. Martin, *Electronic structure: basic theory and practical methods*, Cambridge University Press, Cambridge, 2004.

35 S. Massidda, M. Posternak and A. Baldereschi, Hartree–Fock LAPW approach to the electronic properties of periodic systems, *Phys. Rev. B: Condens. Matter Mater. Phys.*, 1993, **48**, 5058.

36 L. Hedin, New method for calculating the one-particle Green's function with application to the electron-gas problem, *Phys. Rev.*, 1965, **139**, A796.
37 L. Hedin and S. Lundqvist, *Solid state physics*, Academic, New york, vol. 23, 1969.
38 A. Svane and O. Gunnarsson, Transition-metal oxides in the self-interaction-corrected density-functional formalism, *Phys. Rev. Lett.*, 1990, **65**, 1148.
39 V. I. Anisimov, F. Aryasetiawan and A. I. Lichtenstein, First-principles calculations of the electronic structure and spectra of strongly correlated systems: the LDA + U method, *J. Phys.: Condens. Matter*, 1997, **9**, 767–808.
40 M. M. Qazilbash, M. Brehm, B.-G. Chae, P. C. Ho, G. O. Andreev, B.-J. Kim, S. J. Yun, A. V. Balatsky, F. Maple and M. B. Keilmann, *et al.*, Mott transition in VO_2 revealed by infrared spectroscopy and nano-imaging, *Science*, 2007, **318**, 1750–1753.
41 H. Hwang and S. Cheong, Enhanced intergrain tunneling magnetoresistance in half-metallic CrO_2 films, *Science*, 1997, **278**, 1607–1609.
42 H. Sims, S. J. Oset, W. H. Butler, J. M. MacLaren and M. Marsman, Determining the anisotropic exchange coupling of CrO_2 *via* first-principles density functional theory calculations, *Phys. Rev. B: Condens. Matter Mater. Phys.*, 2010, **81**, 224436.
43 M. Pathak, H. Sims, K. B. Chetry, D. Mazumdar, P. R. LeClair, G. J. Mankey, W. H. Butler and A. Gupta, Robust room-temperature magnetism of (110) CrO_2 thin films, *Phys. Rev. B: Condens. Matter Mater. Phys.*, 2009, **80**, 212405.
44 T. Löfwander, R. Grein and M. Eschrig, Is CrO_2 fully spin polarized? Analysis of Andreev spectra and excess current, *Phys. Rev. Lett.*, 2010, **105**, 207001.
45 A. Zaki, The properties and application of scandium-reinforced aluminum, *JOM*, 2003, **55**, 35.
46 S. Tongay, H. Sahin, C. Ko, A. Luce, W. Fan, K. Liu, J. Zhou, Y.-S. Huang, C.-H. Ho and J. Yan, *et al.*, Monolayer behaviour in bulk ReS_2 due to electronic and vibrational decoupling, *Nat. Commun.*, 2014, **5**, 1–6.
47 S. Horzum, D. Çakir, J. Suh, S. Tongay, Y.-S. Huang, C.-H. Ho, J. Wu, H. Sahin and F. M. Peeters, Formation and stability of point defects in monolayer rhenium disulfide, *Phys. Rev. B: Condens. Matter Mater. Phys.*, 2014, **89**, 155433.
48 J. M. Cowley and A. F. Moodie, The scattering of electrons by atoms and crystals. I. A new theoretical approach, *Acta Crystallogr.*, 1957, **10**, 609–619.
49 E. J. Kirkland, *Advanced computing in electron microscopy*, Springer, 2nd edn, 2010.
50 G. Kresse and D. Joubert, From ultrasoft pseudopotentials to the projector augmented-wave method, *Phys. Rev. B: Condens. Matter Mater. Phys.*, 1999, **59**, 1758.
51 J. P. Perdew, K. Burke and M. Ernzerhof, Generalized gradient approximation made simple, *Phys. Rev. Lett.*, 1996, **77**, 3865.
52 S. Grimme, Semiempirical GGA-type density functional constructed with a long-range dispersion correction, *J. Comput. Chem.*, 2006, **27**, 1787–1799.
53 H. J. Monkhorst and J. D. Pack, Special points for Brillouin-zone integrations, *Phys. Rev. B: Solid State*, 1976, **13**, 5188.
54 H. Hellmann, *Einführung in die quantenchemie*, Leipzig, 1937.
55 R. P. Feynman, Forces in molecules, *Phys. Rev.*, 1939, **56**, 340.
56 S. L. Dudarev, G. A. Botton, S. Y. Savrasov, C. J. Humphreys and A. P. Sutton, Electron-energy-loss spectra and the structural stability of nickel oxide: an LSDA + U study, *Phys. Rev. B: Condens. Matter Mater. Phys.*, 1998, **57**, 1505.
57 E. R. Ylvisaker, W. E. Pickett and K. Koepernik, Anisotropy and magnetism in the LSDA + U method, *Phys. Rev. B: Condens. Matter Mater. Phys.*, 2009, **79**, 035103.
58 C. Loschen, J. Carrasco, K. M. Neyman and F. Illas, First-principles LDA + U and GGA + U study of cerium oxides: dependence on the effective U parameter, *Phys. Rev. B: Condens. Matter Mater. Phys.*, 2007, **75**, 035115.
59 P. A. Ignatiev, N. N. Negulyaev, D. I. Bazhanov and V. S. Stepanyuk, Doping of cobalt oxide with transition metal impurities: *ab initio* study, *Phys. Rev. B: Condens. Matter Mater. Phys.*, 2010, **81**, 235123.
60 R. F. W. Bader, *Atoms in molecules. A quantum theory*, Clarendon Press, Oxford, 1994.
61 R. F. W. Bader, Atoms in molecules, *Acc. Chem. Res.*, 1985, **18**, 9–15.
62 R. F. W. Bader, A quantum theory of molecular structure and its applications, *Chem. Rev.*, 1991, **91**, 893–928.
63 R. P. Sagar, A. C. T. Ku, V. H. Smith, Jr. and A. M. Simas, The Laplacian of the charge density and its relationship to the shell structure of atoms and ions, *J. Chem. Phys.*, 1988, **88**, 4367.
64 Z. Shi and R. J. Boyd, The shell structure of atoms and the Laplacian of the charge density, *J. Chem. Phys.*, 1988, **88**, 4375.
65 S. Baroni, P. Giannozzi and A. Testa, Green's-function approach to linear response in solids, *Phys. Rev. Lett.*, 1987, **58**, 1861.
66 P. Giannozzi, S. de Gironcoli, P. Pavone and S. Baroni, *Ab initio* calculation of phonon dispersions in semiconductors, *Phys. Rev. B: Condens. Matter Mater. Phys.*, 1991, **43**, 7231.
67 L. Pauling, Atomic radii and interatomic distances in metals, *J. Am. Chem. Soc.*, 1947, **69**, 542–553.
68 N. Lu, H. Guo, L. Li, J. Dai, L. Wang, W.-N. Mei, X. Wu and X. C. Zeng, MoS_2/MX_2 heterobilayers: bandgap engineering *via* tensile strain or external electric field, *Nanoscale*, 2014, **6**, 2879–2886.
69 C. Ataca, H. Şahin, E. Aktürk and S. Ciraci, Mechanical and electronic properties of MoS_2 nanoribbons and their defects, *J. Phys. Chem. C*, 2011, **115**, 3934–3941.
70 A. N. Andriotis and M. Menon, Tunable magnetic properties of transition metal doped MoS_2, *Phys. Rev. B: Condens. Matter Mater. Phys.*, 2014, **90**, 125304.
71 C. Espejo, T. Rangel, A. H. Romero, X. Gonze and G.-M. Rignanese, Band structure tenability in MoS_2 under interlayer compression: a DFT and GW study, *Phys. Rev. B: Condens. Matter Mater. Phys.*, 2013, **87**, 245114.

72 R. F. W. Bader, *Atoms in molecules. A quantum theory*, Clarendon Press, Oxford, 1994.

73 R. F. W. Bader, Atoms in molecules, *Acc. Chem. Res.*, 1985, **18**, 9–15.

74 R. F. W. Bader, A quantum theory of molecular structure and its applications, *Chem. Rev.*, 1991, **91**, 893–928.

75 R. P. Sagar, A. C. T. Ku, V. H. Smith, Jr. and A. M. Simas, The Laplacian of the charge density and its relationship to the shell structure of atoms and ions, *J. Chem. Phys.*, 1988, **88**, 4367.

76 Z. Shi and R. J. Boyd, The shell structure of atoms and the Laplacian of the charge density, *J. Chem. Phys.*, 1988, **88**, 4375.

77 R. P. Sagar, A. C. T. Ku, V. H. Smith, Jr and A. M. Simas, The Laplacian of the charge density and its relationship to the shell structure of atoms and ions, *J. Chem. Phys.*, 1988, **88**, 4367–4374.

78 P. Ravindran, R. Vidya, A. Kjekshus, H. Fjellvåg and O. Eriksson, Theoretical investigation of magnetoelectric behavior in $BiFeO_3$, *Phys. Rev. B: Condens. Matter Mater. Phys.*, 2006, **74**, 224412.

79 P. h. Ghosez, J.-P. Michenaud and X. Gonze, Dynamical atomic charges: the case of ABO_3 compounds, *Phys. Rev. B: Condens. Matter Mater. Phys.*, 1998, **58**, 6224–6240.

80 K.-W. Lee and W. E. Pickett, Born effective charges and infrared response of LiBC, *Phys. Rev. B: Condens. Matter Mater. Phys.*, 2003, **68**, 085308.

81 M. Posternak, R. Resta and A. Baldereschi, Role of covalent bonding in the polarization of perovskite oxides: the case of $KNbO_3$, *Phys. Rev. B: Condens. Matter Mater. Phys.*, 1994, **50**, 8911.

82 W. Zhong, R. D. King-Smith and D. Vanderbilt, Giant LO–TO splittings in perovskite ferroelectrics, *Phys. Rev. Lett.*, 1994, **72**, 3618.